



Black phosphorus supported Ni₂P co-catalyst on graphitic carbon nitride enabling simultaneous boosting charge separation and surface reaction

Ramireddy Boppella, Wooseok Yang, Jeiwan Tan, Hyeok-Chan Kwon, Jaemin Park, Jooho Moon*

Department of Materials Science and Engineering Yonsei University, 50 Yonsei-ro, Seodaemun-gu, Seoul, 03722, Republic of Korea



ARTICLE INFO

Keywords:

Black phosphorus
Graphitic carbon nitride
Co-catalyst
Nickel phosphide
Hydrogen production

ABSTRACT

Rational design and engineering of highly active co-catalysts made of stable and earth-abundant elements is essential to boost the photocatalytic water splitting performances. This paper reports a 2D-black phosphorus (BP) supported Ni₂P (2D-Ni₂P@BP) as a non-precious heterostructure co-catalyst coupled with a 2D porous graphitic carbon nitride nanosheet (CN NSs) photocatalyst to induce visible light photocatalytic hydrogen production. The resulting 2D-Ni₂P@BP/CN composite structure exhibits a remarkable visible light photocatalytic H₂ evolution activity of 858.2 μmol h⁻¹ g⁻¹, revealing ~50- and ~5-fold enhancement compared to that of a pristine CN reference and Pt/CN sample, respectively. The dramatic advancement in H₂ evolution could be ascribed to the superior hydrogen evolution reduction (HER) activity of Ni₂P@BP. The excellent HER activity arises from the synergistic effect between BP and Ni₂P in which BP, with its superior electron mobility, is believed to accelerate the charge separation/transfer by mediating the photogenerated electrons from CN NSs to the surface of the catalytically active sites of Ni₂P, while Ni₂P promotes the surface reduction reaction by lowering the H₂-evolution overpotential. It is considered that this work provides a new paradigm for designing advanced, stable, and cost-effective photocatalyst systems for the practical implementation of solar hydrogen production.

1. Introduction

Renewable H₂ production from photocatalytic water splitting is one of the most sustainable and attractive strategies to solve the ever-growing global energy demands [1–5]. Despite the tremendous advancement achieved in this area in the past decades, the water splitting efficiency obtained thus far is not high enough for practical implementation on large-scale applications [6–8]. Among the numerous photocatalysts studied, graphitic carbon nitride, comprising earth-abundant elements (C and N), is a potential candidate for photocatalytic H₂ production [9–12]. However, the low surface area, insufficient reaction sites, and severe charge recombinations are believed to hamper the water splitting performance of CN photocatalysts [13,14]. To achieve high quantum efficiency from a CN based photocatalyst, co-catalyst incorporation is considered a fascinating strategy as it can provide active sites for the catalytic redox reactions, thus lowering the overpotential and in turn enhancing charge separation [15,16]. Unfortunately, the most efficient co-catalysts reported so far are dominated by noble metals, and the extreme scarcity of these co-catalysts impedes the commercialization of H₂ producing photocatalysts.

Recently, transition metal phosphides (TMPs) (such as CoP [17], Ni₂P [18], FeP [19], MoP [20], and FeMnP [21]) have emerged as the next generation of highly efficient co-catalysts for photocatalytic water splitting owing to their robust electrochemical hydrogen evolution reaction (HER) and oxygen evolution reaction (OER) [22]. Despite the rapid progress witnessed by the TMP-based co-catalysts during the past few years, several major problems still arise when integrating them into a photocatalyst. For example, (i) lack of intimate interface between the photocatalyst and co-catalysts hinders the interfacial charge transfer [23]; (ii) small particle size with small contact area reduces the charge separation efficiency [24,25]; and (iii) inefficient electron transportation owing to the poor electrical conductivity restricts co-catalytic activity [26,27]. To resolve these shortcomings, the coupling of two-dimensional (2D) conducting materials with high electron mobility has been realized as a promising route to tailor the properties of composite photocatalysts [26,28–31]. Among the various 2D materials, 2D black phosphorus (BP) is an earth-abundant element that possesses numerous exceptional physicochemical properties such as large surface area, remarkably high charge carrier mobility, and long charge-carrier diffusion paths [32–34]. These unique features offer great opportunities for BP to become the new building block of hybrid-structure materials,

* Corresponding author.

E-mail address: jmoon@yonsei.ac.kr (J. Moon).

capable of modulating the electronic properties of these hybrid materials [30,35]. For instance, recent studies have found that BP nanosheets (NSs) can be directly used as a photocatalyst and co-catalyst for H₂ evolution [36–39]. In addition, exploratory works highlight that the BP NSs supported TMPs (denoted as TMPs@BP) have proven to be a potential electrocatalyst for water electrolysis to produce both H₂ and O₂ [24,40,41]. However, to the best of our knowledge, heterostructured Ni₂P@BP based materials have not been explored as a co-catalyst for improving water splitting performance.

Herein, a novel heterostructured 2D-Ni₂P@BP co-catalyst combined with a classical CN photocatalyst is proposed to boost the photo-catalytic H₂ evolution under visible light. Under the optimized conditions, the resulting 2D-Ni₂P@BP/CN showed a remarkable H₂ evolution rate of 858.2 μmol h⁻¹ g⁻¹, exhibiting even higher H₂ evolution than that of the Pt loaded CN, while exhibiting long-term stability for practical applications. Unlike the other conventional TMPs, our 2D-Ni₂P@BP revealed advantageous properties as a high potential co-catalyst: (i) the TMPs attached on BP NSs prevent the agglomeration when they are integrated into photocatalysts, while maintaining high surface area and offering more active catalytic sites for H₂ reduction; ii) the large surface area with 2D structure increases the contact area for interfacial charge transfer, which effectively improves the charge separation efficiency; and (iii) the high conductivity of BP NSs improves the conductivity of Ni₂P, which effectively transfers the charge carriers to the photocatalyst surface and enhances the photocatalytic activity. The photocatalytic and electrochemical results have demonstrated that the coupling of 2D-Ni₂P@BP co-catalyst with 2D-CN NSs plays a vital role in not only improving the charge separation and transfer process but also accelerating the surface reduction reaction.

2. Experimental section

2.1. Synthesis of graphitic carbon nitride (CN)

The mesoporous CN NSs were synthesized by thermal poly-condensation of urea. A known amount of urea was first dissolved in deionised water, and then water was evaporated at 90 °C. The obtained powder was transferred to a crucible covered with a lid and heated under static air at 500 °C for 2 h in a muffle furnace with a heating rate of 10 °C min⁻¹. The resulting mesoporous CN nanosheets were washed with water for several times and dried at 60 °C.

2.2. Preparation of BP nanosheets (NSs)

Bulk BP nanocrystals were directly purchased from Smart Element (Australia). BP NSs were prepared by the sonication-assisted solvent exfoliation method. First, 50 mg of bulk BP nanocrystals was added to 100 mL of anhydrous DMF and bubbled with argon gas to eliminate the dissolved oxygen molecules to prevent the oxidation of BP crystals. The mixture was sonicated for 4 h by using ultrasonicator bath while maintaining the temperature at 0 °C. The resulting brown dispersion was centrifuged at 2000 rpm for 30 min to remove the bulk BP nanocrystals and obtain BP NSs.

2.3. Preparation of Ni₂P@BP NSs

Ni₂P@BP NSs were prepared via a solvothermal method as described in the literature [24]. The required amount of NiCl₂·6H₂O was added to 50 mL of the above synthesized BP NSs in anhydrous DMF solution and sonicated for 30 min to obtain a transparent solution. The suspension was transferred into a 125 mL Teflon-lined stainless steel autoclave (Acid Digestion Vessel, Parr Instrument Company, Moline, IL, USA), and heat-treated at 160 °C for 3 h. The obtained black colored Ni₂P@BP NSs was collected after washing with absolute ethanol for several times, and dried at 60 °C in a vacuum oven. The weight ratio of BP to Ni was varied by adding different amounts of NiCl₂ to the BP NSs.

The actual weight ratio of P to Ni was measured by inductively coupled plasma mass spectrometry (ICP-MS, Agilent-7900) and the results are summarized in Table S1.

2.4. Preparation of Ni₂P@BP/CN hetero-nanostructures

First, the synthesized mesoporous CN NSs were dispersed in anhydrous DMF under ultra-sonication for 3 h to form a homogeneous dispersion. Then, the known amount of Ni₂P@BP NSs was added to the above CN dispersion and subjected to hydrothermal treatment for 3 h at 160 °C. The resulting Ni₂P@BP/CN NSs were collected by washing with ethanol, and dried at 60 °C in a vacuum oven. The weight ratio of CN to Ni₂P@BP was varied by adding different amounts of CN to the Ni₂P@BP NSs, and the corresponding samples were denoted as Ni₂P@BP/CN (1 wt%), Ni₂P@BP/CN (2 wt%), and Ni₂P@BP/CN (3 wt%). BP/CN nanostructures were also synthesized by the same procedure, except that BP NSs were added to CN NSs instead of Ni₂P@BP NSs. Ni₂P/CN was prepared according to the previous report with a slight modification [42], and the detailed experimental procedure is described in Supplementary Information. For the purpose of photocatalytic activity comparison, CN NSs were also solvothermally treated with anhydrous DMF solution at 160 °C for 3 h. The physicochemical properties of the synthesized photocatalysts were thoroughly analyzed by various characterization techniques, as described in Supplementary Information.

2.5. Photocatalytic H₂ evolution

The photocatalytic reaction was carried out in a 70 mL cylindrical quartz reactor with irradiation area of ~13 cm². A total amount of 20 mg of Ni₂P@BP/CN photocatalyst was dispersed in 40 mL of aqueous solution containing 10 vol% of TEOA in a reaction cell. The resulting suspension was sealed with rubber stamp and deaerated with N₂ gas for 30 min to remove the dissolved molecular gases. The reaction cell was irradiated with a 300 W xenon lamp equipped with a 420 nm cut-off filter (20CGA-420, Newport Corporation, Irvine, CA, USA), and the focused light intensity on the reactor was adjusted to ~100 mW cm⁻² using a certified Si reference cell (Newport Corporation, Irvine, USA). The evolved gas products were determined with a gas chromatograph (6500GC system, YL instrument, Anyang, Korea) equipped with a MS-5 A column and pulsed discharge detector. For the stability experiments, the photocatalysts were collected after the first cycle and re-dispersed into 40 mL of a water–TEOA solution for the next round. The photocatalytic reaction over Pt/CN was conducted under the same condition except for the addition of a certain amount of H₂PtCl₆ to the CN, followed by photo-deposition of the Pt co-catalyst. The apparent quantum efficiency was measured under the irradiation of 420 nm monochromatic light. The apparent quantum yield (AQE) was obtained from the following equation;

$$\text{AQE} = \frac{2 \times \text{The number of evolved H}_2 \text{ molecules}}{\text{The number of incident photons}} \times (100) \quad (1)$$

2.6. Electrochemical (EC) and photoelectrochemical (PEC) measurements

The PEC properties of the as-prepared photoelectrodes were characterized with a three-electrode configuration using a potentiostat (SI 1287, Solartron, Leicester, UK). The photoelectrodes were used as working electrodes, the Ag/AgCl (KCl saturated) as the reference electrode, and Pt wire was used as counter electrodes. The photoelectrodes were prepared by spin coating (2000 rpm min⁻¹, 30 s) of a catalyst suspension onto the surface of a fluorine doped tin oxide (FTO) plate (2 × 2 cm²) and dried at 150 °C in a glove box. The spin coating process was repeated five times to obtain the desired thickness. The catalyst suspension was prepared by adding 20 mg of catalyst into 5 mL of ethanol and 0.05 mL of Nafion mixed solution. A 300 W Xenon lamp with a UV cut-off filter (> 420 nm) was used as the light source, and

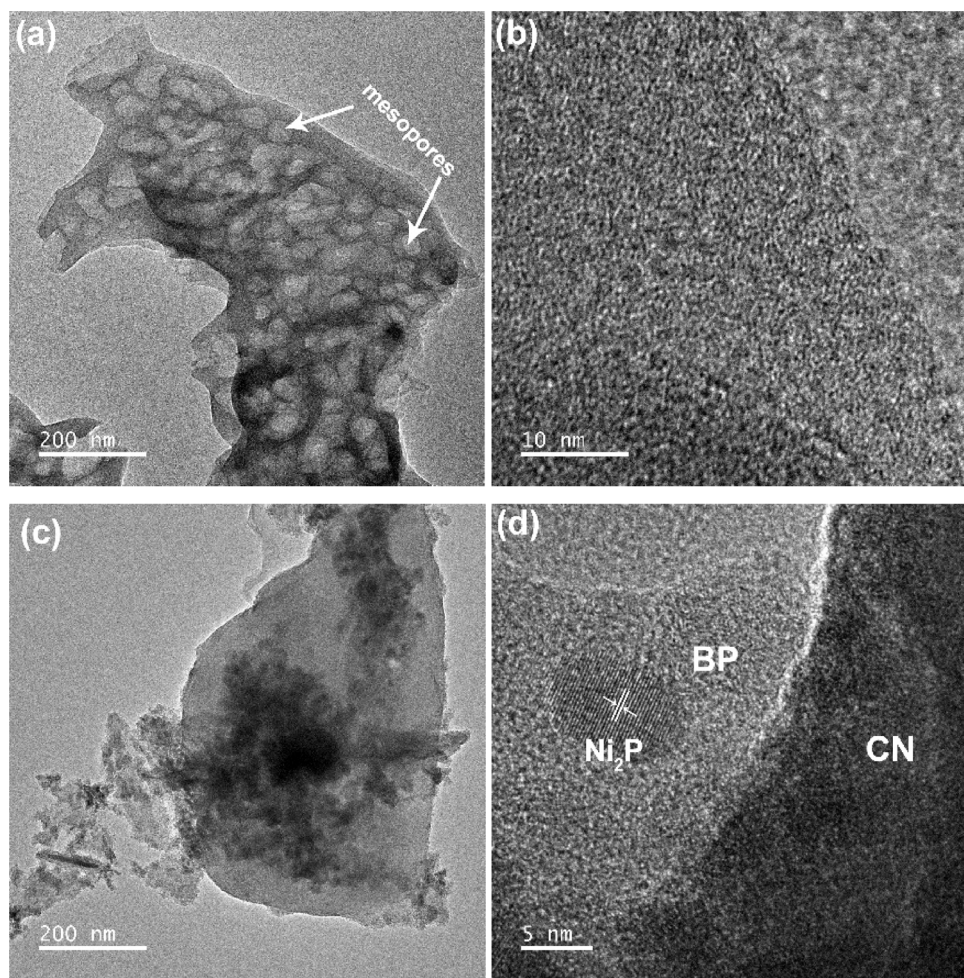


Fig. 1. (a) TEM image and (b) HR-TEM image of CN NSs. (c) TEM image and (d) HR-TEM image of Ni₂P@BP/CN.

0.5 M Na₂SO₄ solution was used as the electrolyte. The electrochemical impedance spectroscopy (EIS) measurements were conducted in the same three-electrode system over a range from 0.01 to 10⁵ Hz with an AC amplitude of 10 mV at an applied potential of 0.3 V vs. Ag/AgCl under visible light irradiation ($\lambda > 420$ nm). The polarization curves were recorded in the above-mentioned three-electrode system, except the catalysts deposited on a glassy carbon (GC) electrode that was used as working electrode, and the bias sweep range was from –1.5 to –0.8 V versus Ag/AgCl (saturated KCl) with a step size of 5 mV. A 0.5 M H₂SO₄ and 0.5 M Na₂SO₄ aqueous solution was utilized as electrolyte and 0.005 mL of the above suspension was dropped onto the surface of a GC electrode (3 × 3 mm) and dried in ambient condition.

3. Results and discussion

The BP NSs were obtained by sonication-assisted solvent exfoliation of bulk BP single crystals. Ni₂P@BP NSs were then obtained by a solvothermal treatment of ultrathin BP NSs in anhydrous dimethylformamide (DMF) solution containing the desired amount of Ni ions at 160 °C for 3 h. The phase composition of BP and Ni₂P@BP NSs was first confirmed by the X-ray diffraction (XRD) pattern. As shown in Fig. S1, the sharp peaks at 16.96, 26.59, 34.27, 40.1, and 52.45 correspond to the crystal planes of (020), (021), (040), (041), and (060) respectively, indicating the high crystallinity of black phosphorous (JCPDS card no.73-1358), and no other crystalline impurities were detected. Besides, a series of new diffraction peaks was found after the solvothermal reaction of BP with Ni ions at 40.58, 42.9, and 44.58 (Fig. S1), which can be indexed to the (111), (021), and (210) planes of the

hexagonal structure Ni₂P (JCPDS NO. 65-3544), respectively. These data clearly showed that the samples exhibit typical XRD peaks for both BP and Ni₂P, confirming that Ni₂P was successfully grown on the BP NSs [24,40]. Raman spectroscopy of the bulk BP disclosed three phonon-modes located at 361.5 (A_g¹), 439 (B_{2g}), and 466.3 cm^{−1} (A_g²) (Fig. S2) [24,40]. The peaks were red shifted after exfoliation (*i.e.*, BP NSs), suggesting the thickness reduction. However, these three-phonon modes were blue-shifted after Ni₂P was grown on the BP NSs (*i.e.*, Ni₂P@BP NSs) owing to the vibration inhibition, which is in good accordance with previous observations [40].

The detailed morphological studies of BP and Ni₂P@BP NSs were analyzed by transmission electron microscopy (TEM). As shown in Fig. S3a, the exfoliated BP NSs showed thin nanosheet morphology with a size of several hundred nanometers. Well-resolved lattice fringes were clearly observed from the high-resolution TEM (HR-TEM) images with a *d*-spacing of 0.25 nm matching to the (040) plane of BP (Fig. S3b), which is in good accordance with the XRD analysis. In the TEM images of Fig. S3c, the as-prepared Ni₂P@BP heterostructure displays a typical 2D-morphology, and copious amount of ultra-small Ni₂P crystallites were evenly dispersed on the surface of the BP NSs. The tiny size of the Ni₂P nanocrystals supported on BP NSs endowed a high surface-to-volume ratio and a large number of exposed catalytic active sites are readily available to take part in the photocatalytic reaction [43]. The detailed HR-TEM image of Ni₂P@BP presents the two sets of lattice fringes, of 0.259 nm and 0.224 nm (Fig. S3d), which agree well with the (040) plane of BP (JCPDS card no. 74-1878) and (111) plane of Ni₂P (JCPDS card no. 65-3544), respectively. The elemental mapping of an individual nanosheet obtained by energy-dispersive X-ray spectroscopy

(EDS) further confirmed the homogeneous distribution of the Ni and P elements throughout the whole nanosheet (Fig. S4). Besides, the thickness of exfoliated BP and Ni₂P@BP NSs was analyzed by the atomic force microscopy (AFM). The AFM images of exfoliated BP as well as the Ni₂P@BP nanosheets showed the thicknesses of 14 nm and 21 nm, respectively (Fig. S5).

The as-synthesized Ni₂P@BP NSs were combined with CN NSs by a facile solvothermal method to establish a strong electronic interaction in the heterostructured Ni₂P@BP/CN nanocomposites. The physicochemical properties of the as-synthesized samples were investigated by extensive characterizations techniques. The XRD pattern of CN exhibits two diffraction peaks at around 13.1° and 27.4° corresponding to the (100) and (002) planes (JCPDS#87-1526), which are characteristic peaks of the in-planar structural packing of tri-s-triazine units and interplanar stacking of an aromatic system, respectively (Fig. S6) [44]. After hybridization of CN NSs by Ni₂P@BP, CN retained its basic structure in Ni₂P@BP/CN composites and no obvious diffraction peaks corresponding to the Ni₂P@BP NSs were detected, possibly because of the small loading amount of Ni₂P@BP on CN NSs. The TEM images of Fig. 1a present the typical 2D nanosheet structure of CN, possessing mesoporous structures with a lateral size of several hundred nanometers. The HR-TEM image shows the typical amorphous phase of CN (Fig. 1b). After hybridization with BP@Ni₂P, a representative TEM analysis shows that the Ni₂P@BP NSs flatly adhered to the surface of CN NSs (Fig. 1c). The high-resolution TEM image reveals a close interfacial contact between Ni₂P@BP NSs and CN NSs (Fig. 1d). Additional EDS elemental mapping images further verified the homogeneous distribution of C, N, P, and Ni elements in the Ni₂P@BP/CN composite (Fig. S7). These TEM results along with EDS mapping images demonstrated that Ni₂P@BP NSs are intimately contacted with 2D CN NSs without any spatial separation. The intimate interface formed between the Ni₂P@BP NSs and CN NSs could facilitate the charge transfer across the interface because of the shortened transfer distance of the photo-generated charge carriers and anticipate an appreciable improvement in photocatalytic activity [23,45].

The surface area and pore textural properties of the composite samples were determined by a Brunauer–Emmett–Teller (BET) analysis (Fig. S8), and the detailed parameters are listed in Table S2. All the samples exhibit a typical type IV isotherm, indicating their mesoporous nature [46]. The BET surface area of CN ($96.21 \text{ m}^2 \text{ g}^{-1}$) was decreased to $75.05 \text{ m}^2 \text{ g}^{-1}$ and $41.26 \text{ m}^2 \text{ g}^{-1}$ after BP and BP@Ni₂P loading, respectively. It can be speculated that the incorporation of BP and BP@Ni₂P covering most of the mesopores present in the CN NSs leads to the reduction in specific surface area. Fourier-transform infrared (FTIR) spectroscopy was employed to investigate the chemical bonding among the components of the synthesized samples (Fig. S9). The peaks centered between 3100–3300 cm⁻¹ originate from the N–H stretching vibration and adsorbed water species on the CN surface [47,48]. The bands between 1200–1600 cm⁻¹ could be ascribed to the typical C–N stretching modes of heterocycles, and the other strong peak located at 807 cm⁻¹ was related to the breathing mode triazine ring [47,48]. No IR signals relative to Ni₂P@BP could be detected in the composite structures and no deformation of the original CN backbones was observed after hybridization, confirming the no obvious chemical interaction between CN and Ni₂P@BP.

To study in-depth the surface chemical structure between CN and Ni₂P@BP, high-resolution X-ray photoelectron spectroscopy (XPS) measurements were performed. Fig. 2a revealed that the C 1s spectra of the CN sample exhibit the three major peaks centered at 288.02 eV, 286.14 eV, and 284.60 eV, which can be assigned to the typical N–C = N bonding configuration, sp³-bonded carbon (N–C) species, and graphitic carbon (C=C), respectively [42]. The C 1s peak of BP/CN and Ni₂P@BP/CN was shifted 0.11 eV toward higher binding energy compared to that of pristine CN. Meanwhile, the N 1s spectra, which exhibit binding energies at 398.39, 399.78, and 404.33 eV, could be assigned to the sp²-hybridized nitrogen in CN = C, tertiary nitrogen (N–

(C)₃), and charging effects of C–N–H, respectively [42]. It is worth mentioning that the N 1s peaks of Ni₂P@BP/CN and BP/CN (Fig. S10) shifted toward higher binding energies compared with that of N 1s peaks in pure CN, manifesting the strong electronic interaction between Ni₂P@BP and BP with CN.

The Ni 2p core-level spectrum of Ni₂P@BP exhibited four strong peaks in the Ni 2p_{3/2} region with binding energies of 853.43, 856.8, 862.05, and 865.7 eV (Fig. 2c), which are related to the characteristic Ni^{δ+} ($0 < \delta < 2$) in the Ni₂P phase, oxidized Ni species, and satellite peak of the Ni^{δ+} and Ni(II), respectively [48–50]. In addition, Ni 2p_{1/2} spectra showed other four peaks at 870.62, 874.39, 878.87, and 883.01 eV, which could be ascribed to Ni^{δ+} in Ni₂P, oxidized Ni species, and the satellites of the Ni 2p_{1/2} peak, respectively [48–50]. Upon introduction of Ni₂P@BP into CN, the binding energy of Ni 2p was shifted ~ 0.6 eV to a lower binding region, which is consistent with the positive shift of C1s and N1s of Ni₂P@BP/CN. Such positive (CN) and negative shift (Ni₂P@BP) in binding energy indicates a transfer of electron density from CN to Ni₂P@BP owing to strong electronic interactions between Ni₂P@BP and CN [51]. To elucidate the formation of Ni₂P on BP structures, XPS spectra of P 2p were measured and compared with the BP structure. The deconvoluted P 2p spectra of Ni₂P@BP disclose three strong peaks at 129.14, 129.96, and 133.0 eV, which are assigned to P 2p_{3/2}, P 2p_{1/2}, and the oxidized species on the surface PO₄³⁻, respectively (Fig. 2d). The peak at 129.48 was shifted to lower binding energy for Ni₂P@BP, indicating that a negative valence of P^{δ-} further confirms the formation of metal–phosphorus bond in accordance to previous results [52]. The high-resolution P 2p spectra of Ni₂P@BP/CN showed much stronger PO₄³⁻ compared to BP NSs, which is likely due to the partial oxidation of BP during the multiple preparation processes [53]. It is worth mentioning that the P 2p peak for Ni₂P@BP/CN further shifted towards lower binding energies, and this shift may further suggest an electron transfer from the CN to Ni₂P@BP.

The photocatalytic H₂-production activity of the as-synthesized samples was examined in 10 vol% triethanol amine (TEOA) aqueous solution under visible-light irradiation (> 420 nm). As shown in Fig. 3a, pure BP NSs revealed no H₂ activity owing to the high charge recombination (the result is not shown here), while the Ni₂P@BP exhibited obvious photocatalytic H₂ evolution owing to a co-catalytic effect of Ni₂P, similar to that in the previous report [54]. A trace amount of H₂ (17.2 $\mu\text{mol g}^{-1} \text{ h}^{-1}$) was detected when pure CN was used. With the loading of BP, the BP/CN sample gave rise to a slightly increased H₂ production activity of 116.19 $\mu\text{mol g}^{-1} \text{ h}^{-1}$. These results indicate that the introduction of BP NSs can enhance the photocatalytic activity up to certain degree by forming the heterojunction [37,38]. The loading of 1 wt% Ni₂P@BP on CN drastically enhanced the photocatalytic H₂ evolution activity up to 673.03 $\mu\text{mol g}^{-1} \text{ h}^{-1}$. By further increasing the Ni₂P@BP amount, the photocatalytic activity of Ni₂P@BP/CN was gradually enhanced. A superior photocatalytic H₂-production activity of 858.2 $\mu\text{mol g}^{-1} \text{ h}^{-1}$, corresponding to a quantum efficiency (QE) of 2.8% at 420 nm, was achieved with the loading of 2 wt% Ni₂P@BP, thus outperforming CN by an exceptional factor of 50.5. The superior H₂ production activity of Ni₂P@BP/CN photocatalysts can be attributed to the cooperative effect of the following factors: (i) the BP NSs, with their superior electron mobility, form a heterojunction with the CN NSs, facilitating the rapid separation and transportation of the electron-hole pairs in CN, and (ii) the Ni₂P deposited on BP NSs serves as catalytically active sites to produce H₂ from water reduction reaction by lowering the H₂ overpotential required for water splitting. Besides, higher loading of Ni₂P@BP decreased the H₂ evolution rate owing to the excessive Ni₂P@BP coverage of the active sites on CN. Though Ni₂P@BP NSs alone showed decent H₂ production activity under visible-light irradiation, the overloading of BP@Ni₂P may also hinder the light adsorption of CN and reduce the photoactivity [38,53].

To evaluate the impact of BP support in the heterostructured Ni₂P@BP co-catalyst on H₂ evolution activity, Ni₂P nanocrystals were directly synthesized on CN NSs without BP support. The resulting Ni₂P/CN

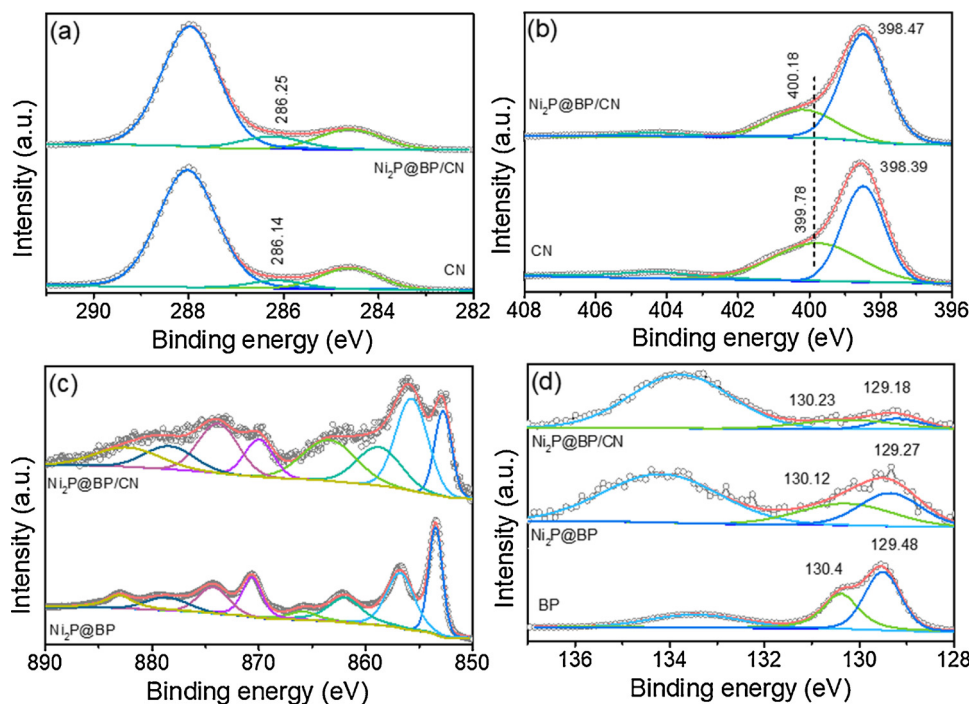


Fig. 2. XPS spectra of (a) N 1s, (b) C 1s, (c) Ni 2P, and (d) P 2P for various samples of CN, BP, Ni₂P@BP, BP/CN, and Ni₂P@BP/CN.

heterostructures exhibited lower photocatalytic H₂ activity (376.3 μmol g⁻¹ h⁻¹) than that of Ni₂P@BP/CN. It has been reported that both Ni₂P [55,56] and BP NSs [37,53] have proven to be efficient H₂ reduction co-catalysts (HER) for CN. However, the HER activity of BP and Ni₂P utilized in the present study is incomparable with that of our heterostructured Ni₂P@BP co-catalyst under the same experimental condition. The photocatalytic HER activity of these co-catalysts underscores the robust co-catalytic activity of Ni₂P@BP. Indeed, the Ni₂P@BP exhibited excellent HER activity (Fig. S11a) and high electrical conductivity (Fig. S11b) compared to that of pristine BP and Ni₂P nanoparticles. The high co-catalytic activity of Ni₂P@BP could be attributed to a synergistic effect between Ni₂P and BP, in which the BP NSs are believed to improve the charge separation efficiency and Ni₂P promotes the surface redox reactions [24,41,54]. Meanwhile, the superior activity of Ni₂P@BP/CN was attributed to the strong interfacial interaction formed between the CN and Ni₂P@BP entrenched during the solvothermal treatment, which markedly speeds up the interfacial charge transfer. It is also worth to note that the H₂ evolution rate was ~5 times higher than that of Pt/CN with similar Pt loading (166.85 μmol g⁻¹ h⁻¹), even though Pt is known as the benchmark co-catalyst for H₂ production. The photocatalytic H₂ production activity of our Ni₂P@BP/CN also surpass that of most of the TMP integrated CN based photocatalysts (Table S3). In order to compare the photocatalytic activity of our catalyst with that of the previously reported state-of-the-art

catalysts, the photocatalytic activity was normalized with respect to the irradiation area of the light [57]. The H₂ production rate of Ni₂P@BP/CN (7151 μmol m⁻² h⁻¹) is thus comparable to other highly active CN-based catalysts [55,57].

The effect of the weight ratio of P to Ni in Ni₂P@BP on H₂ evolution was studied while keeping the same total weight amounts of CN to Ni₂P@BP. As shown in Fig. S12, the amount of Ni₂P on BP NSs has an appreciable effect on the activity of the co-catalyst. The optimum mass ratio of P to Ni in the current photocatalytic system was found to be 1:1, giving a H₂ evolution rate of 858.2 μmol g⁻¹ h⁻¹. Further increase in the mass ratio of P to Ni seems to decrease the photocatalytic H₂ activity of the CN photocatalyst. It might be due to the overloading of Ni₂P nanoparticles on the BP NSs surface, which would reduce the catalytic active sites. The stability of the optimized Ni₂P@BP/CN was evaluated for five consecutive cycles for a period of 20 h, under the same experimental conditions. No obvious deterioration of photocatalytic H₂ evolution was observed during the five successive cycling tests, indicating that Ni₂P@BP/CN maintains outstanding stability (Fig. 3b). The crystal structures, morphologies, and chemical composition of the recycled catalysts were further examined by XRD, TEM, and XPS analyses (Fig. S13–S15). No significant alterations were observed in the crystal structure, morphology, and chemical composition after five successive runs of photocatalytic reaction. All these observations further support the robust stability of our Ni₂P@BP/CN

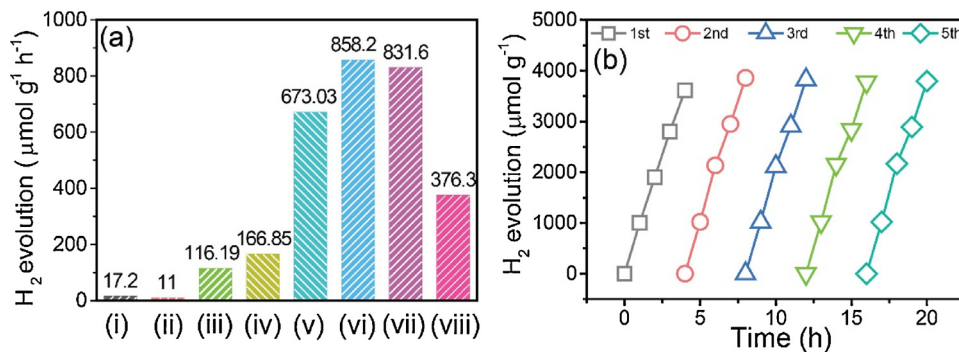


Fig. 3. (a) Photocatalytic H₂ evolution rates over various samples under visible light ($\lambda > 420$ nm) irradiation. (i) CN; (ii) Ni₂P@BP; (iii) BP/CN (2 wt%); (iv) Pt/CN (2 wt%); (v) Ni₂P@BP/CN (1 wt%); (vi) Ni₂P@BP/CN (2 wt%); (vii) Ni₂P@BP/CN (3 wt%); and (viii) Ni₂P/CN. (b) Cycle stability test of H₂ evolution over the Ni₂P@BP/CN (2 wt%) sample under visible light over a period of 20 h for five consecutive runs.

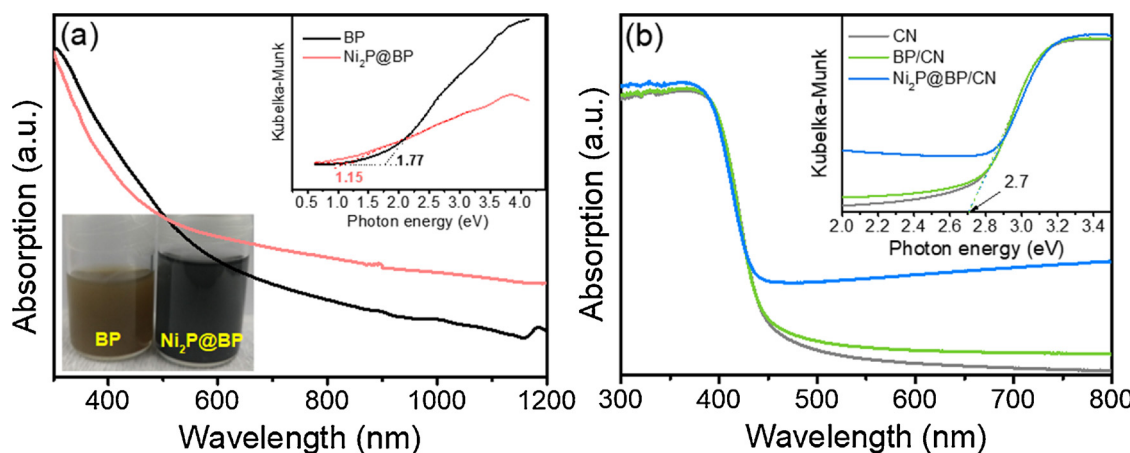


Fig. 4. (a) UV–vis–NIR absorption spectra of BP and Ni₂P@BP and the corresponding Kubelka–Munk function (top inset) and photographs of each sample (bottom inset). (b) UV – vis diffuse absorption spectra of CN, BP/CN, and Ni₂P@BP/CN and the corresponding Kubelka–Munk function (inset).

photocatalyst for water splitting. The general applicability of our heterostructured co-catalysts can also be extended to other transition metals such as Co and Fe (Fig. S16). The synthesized CoP@BP and FeP@BP when deposited onto CN NSs also markedly improved the H₂ evolution performance, which was 47 and 40 times higher than that of bare CN NSs photocatalysts, respectively. These results imply that the heterostructured based TMPs have promising potential as highly active co-catalysts to boost H₂ evolution over different semiconductors.

To investigate the origin of the excellent activity of Ni₂P@BP/CN, the light harvesting capability of Ni₂P@BP/CN was estimated by UV-vis absorption spectra. As showed the absorption spectra in Fig. 4a, BP nanosheets exhibited strong absorption capability in the visible and NIR region (300–1200 nm), corresponding to a band energy of 1.77 eV according to Kubelka–Munk function. After deposition of Ni₂P on BP NSs, the colour of BP NSs turned from brown to black (bottom inset in Fig. 4a), due to the strong electronic coupling between BP NSs and Ni₂P nanoparticles. The intensity of absorption band for Ni₂P@BP significantly increased in visible and NIR region in agreement with the black colored of Ni₂P@BP sample, indicative of the strong absorption capability of Ni₂P@BP. In contrast, pure CN showed an absorption edge at around 459 nm, equivalent to the band gap energy of 2.7 eV (Fig. 4b). Upon the integration of BP and Ni₂P@BP into CN, the light absorption intensity of the resulting BP/CN and Ni₂P@BP/CN was apparently increased in the entire region of 350–800 nm, which is attributed to the superior light absorption of BP and Ni₂P@BP in the entire wavelength region. However, Ni₂P@BP/CN composites revealed more intense absorption in the entire visible region, which is consistent with the observed colour change of the samples. The enlarged light absorption of the composite can maximize the light utilization across the spectrum, thus leading to the generation of additional electron-hole pairs under broad spectrum light. However, there was no significant shift observed in the onset of the absorption edge relative to that of pure CN, implying that the Ni₂P@BP is not doped into the crystal lattice of CN rather than anchored on the surface of CN, which is in accordance with the aforementioned XRD data. To evaluate the possibility of enhanced visible light activity of Ni₂P@BP/CN caused by stronger visible light absorption of Ni₂P@BP NSs, the photocatalytic hydrogen evolution was performed at a wavelength longer than 600 nm. However, no H₂ evolution was detected under such a condition, inferring that the increased absorption of Ni₂P@BP does not promote the photocatalytic activity of Ni₂P@BP/CN. Thus, the improved photoactivity of Ni₂P@BP/CN is believed to come from the two factors of charge separation and rapid transfer, both of which are believed to originate from the large interfacial contact area (Fig. 1c) and high electronic conductivity, as discussed below.

Charge separation and transportation efficiency in our Ni₂P@BP/CN

catalyst was thoroughly investigated by various characterization techniques. First, steady-state photoluminescence (PL) spectra and time-resolved photoluminescence (TRPL) spectra were employed to explore the radiative recombination process and transfer of photogenerated charge carriers. Laser pulses of 375 nm (5 MHz, 0.25 μW, 32 ps resolution) were chosen to excite the photo-generated electrons on both CN and composite photocatalysts. The pristine CN sample showed a strong emission peak at 460 nm, which arises from the recombination of excited electrons-hole pairs in the CN photocatalyst (Fig. 5a). However, the emission peak was significantly decreased upon the introduction of BP with CN to form a heterostructure, suggesting efficient separation and fast transfer of the photo-generated charge carriers from CN to BP. This result provides a solid proof that the binary composite could greatly enlarge the lifetime of photogenerated electron-hole pairs by encouraging the charge migration process through the efficient interface formed between CN and BP NSs. Furthermore, upon loading of Ni₂P@BP into CN, the emission peak was further reduced. The suppression of PL implies longer lifetime of the electron-hole pair and/or faster separation/migration of the charge carrier [58]. To acquire detailed insights into the lifetime of charge carrier dynamics, TRPL decay curves (Fig. 5b) were fitted using the tri-exponential function, as follows [59,60]:

$$I(t) = A_1 \exp(-t/\tau_1) + A_2 \exp(-t/\tau_2) + A_3 \exp(-t/\tau_3) \quad (2)$$

Meanwhile, the average lifetime (τ_{ave}) was calculated using following equation [59,60]

$$\tau_A = \frac{\tau_1^2 A_1 + \tau_2^2 A_2 + \tau_3^2 A_3}{\tau_1 A_1 + \tau_2 A_2 + \tau_3 A_3} \quad (3)$$

where τ_1 , τ_2 , and τ_3 are the emission lifetimes, and A_1 , A_2 , and A_3 are the corresponding amplitudes. In general, the longer decay lifetime component τ_1 is considered to free exciton recombination in the CN and its composites, and the shorter decay lifetime components τ_2 and τ_3 are ascribed to the surface-related nonradiative recombination of the charge carriers [58–60]. As listed in Table S4, the average lifetime of Ni₂P@BP/CN (12 ns) was distinctly enhanced as compared to that of CN (8.6 ns) and CN/BP (9.2 ns). The longer lifetime may be attributed to the suppressed charge recombination and prolonged lifetime of the charge carriers. The quenched PL and longer lifetime of the charge carriers suggest that the presence of Ni₂P@BP can effectively suppress the charge-carrier recombination by effectively separating/transferring the charge-carrier to the surface of Ni₂P@BP/CN [58]. The effective interfacial charge separation in the Ni₂P@BP/CN can be ascribed to the formation of intimate interfaces between CN and Ni₂P@BP, as evidenced in Fig. 1.

To shed more light on the charge-transfer properties,

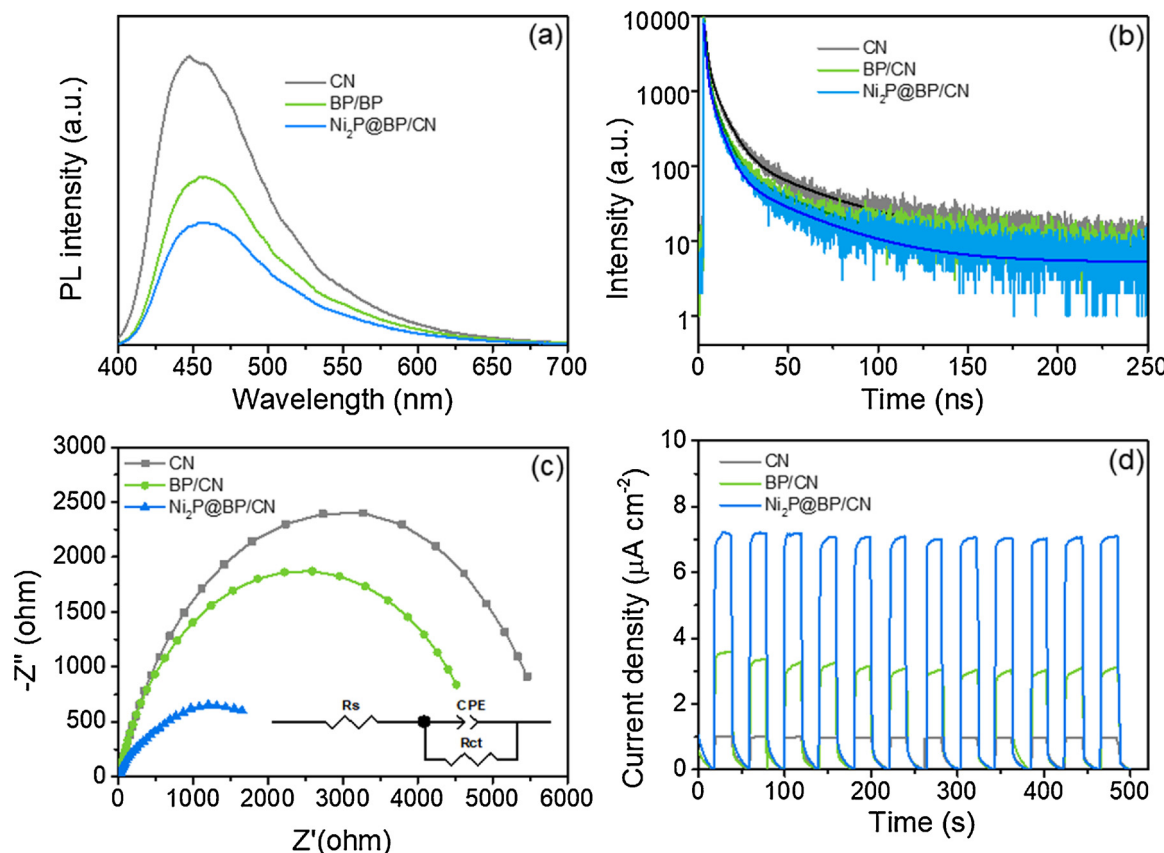


Fig. 5. (a) Study state PL spectra and (b) time-resolved transient PL decay curves of CN, BP/CN, and CN/BP@Ni₂P excited at 375 nm. (c) Nyquist plots of resulting photoelectrodes measured under a bias potential of 0.3 V (vs. Ag/AgCl) potential under visible-light illumination in 0.5 M Na₂SO₄ solution. The symbols show the measured data and the lines represent the fitting results. The inset of (c) displays the equivalent circuit of the photoelectrodes. (d) Transient photocurrent measurements in 0.5 M Na₂SO₄ under a bias potential of 0.3 V (vs. Ag/AgCl) under visible-light irradiation.

electrochemical impedance spectroscopy (EIS) measurements were carried out under visible light illumination (Fig. 5c). A typical equivalent circuit model shown in the inset of Fig. 5c was used for fitting the EIS data, where the R_s, R_{ct}, and CPE represent the series resistance accounting for the transport resistance in the photoelectrochemical cell, the charge transfer resistance associated with recombination of electrons across the Ni₂P@BP/CN/electrolyte interface, and the capacitance at the Ni₂P@BP/CN/electrolyte interface, respectively [61,62]. The EIS results based on the fitted parameters support the conclusion that Ni₂P@BP/CN has smaller semicircle and lower interfacial charge-transfer resistance (2484 Ω) than those of CN (11,512 Ω) and BP/CN (9173 Ω), highlighting the obvious enhancement in the interfacial charge transfer on the surface of Ni₂P@BP/CN [3,29]. Furthermore, transient photocurrent measurements were conducted in the Na₂SO₄ and Na₂SO₃ electrolyte to study the bulk charge transfer in CN, BP/CN, and Ni₂P@BP/CN. The presence of Na₂SO₃ in the electrolyte readily captures the photo-generated hole on the surface of the catalyst, and thus, eliminates the surface recombination. As elucidated in Fig. 5d, the BP/CN exhibited enhanced photocurrent response (3.57 μA cm⁻²) compared to that of pristine CN (1.01 μA cm⁻²), indicating that the hybridization of BP NSS promote the bulk charge separation and transfer. As expected, after the introduction of Ni₂P@BP, the as-prepared composites exhibited higher photocurrent response (7.3 μA cm⁻²) in comparison to that of other counterparts. The boosted photoresponse in the composite is directly manifested by the enhanced bulk charge-separation efficiency on Ni₂P@BP/CN [63]. The reduced bulk charge separation in the BP/CN and Ni₂P@BP/CN system can be ascribed to the intimate contact between CN and BP, which shortens the electron transfer path and in turn leads to the effective separation of electron-holes generated in the bulk CN, thus avoiding the

recombination of all the photo-excited electron-hole pairs in CN.

Besides the charge separation, surface redox reactions are another important factor that determines the photoactivity, which is closely associated with its surface area and active sites. The average specific surface areas of the samples listed in Table S2 revealed that the difference in photocatalytic activity was not influenced by the specific surface area, indicating that surface area has no significant role in improving photocatalytic H₂ evolution activity. Linear sweep voltammetry (LSV) was performed to investigate the surface reduction abilities of synthesized samples in an N₂-saturated 0.5 M Na₂SO₄ solution. As shown in Fig. S17, Ni₂P@BP/CN exhibited high current density and lower overpotential compared to that of CN and BP/CN, further verifying that BP@Ni₂P could speed up the surface reaction for proton reduction. Compared to BP/CN, the higher activity in Ni₂P@BP/CN was attributed to the larger surface reductive active sites of Ni₂P@BP NSS than those of BP NSS. Based on these results, the introduction of Ni₂P@BP co-catalysts can serve as an effective electron regulator to enhance the charge separation and to provide additional reaction sites for surface catalytic reactions, resulting in higher photocatalytic activity.

On the basis of the above photocatalytic and electrochemical analyses, the boosted photoactivity of Ni₂P@BP/CN likely results from effective vectorial charge transfer from bulk CN to the surface of Ni₂P through the conductive BP, and effective reduction of H⁺ to H₂ on the Ni₂P surface. To better understand the underlying photoexcited carrier dynamics involved in the Ni₂P@BP/CN during the photocatalytic process, the band-edge positions of CN, BP, and Ni₂P@BP were studied. The positions of the conduction band (CB) and valence band (VB) of CN, BP, and Ni₂P@BP were evaluated by the combined analyses of the valence band X-ray photoelectron spectroscopy (VB-XPS), Mott-Schottky analysis and UV-vis absorption spectra. Fig. S18a, c, e display

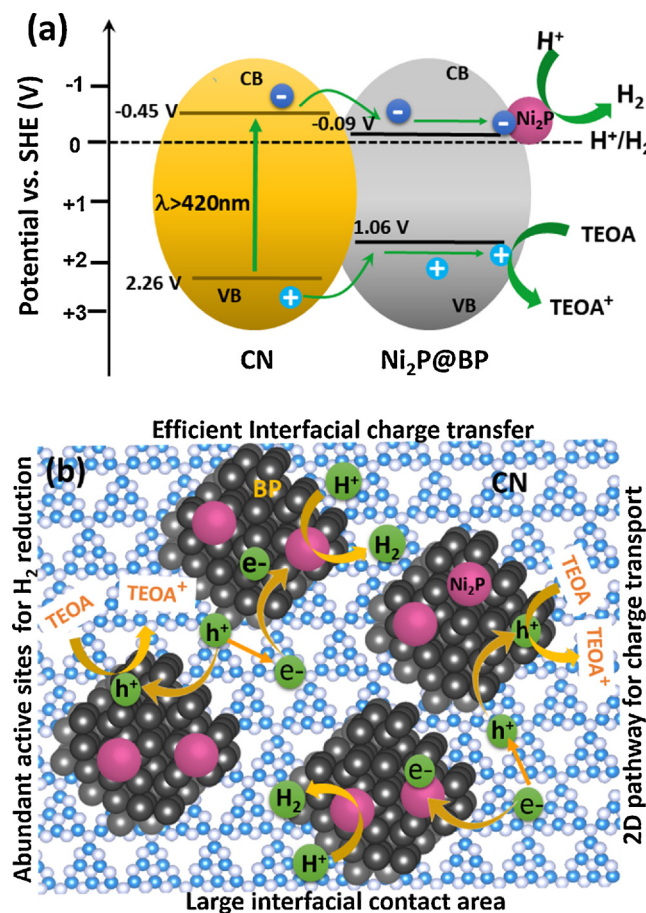


Fig. 6. a) Schematic representation of charge separation and transfer and H₂ production over Ni₂P@BP/CN photocatalyst under visible-light irradiation ($\lambda > 420$ nm). b) The schematic illustration highlights the structural benefits of the Ni₂P@BP/CN photocatalyst and proposed carrier pathway of photoexcited electron generation, migration, and transport under visible-light irradiation.

that the valence band (VB) edge of the CN, BP NSs, and Ni₂P@BP are determined to 2.25, 1.56 and 1.06 eV, respectively. The CB position was then estimated by measuring the flat band potential (E_{fb}) at the intercept of the x-axis through the extrapolation in the Mott-Schottky plot (Fig. S18b, d, f). The EF_b of CN, BP NSs, and Ni₂P@BP were found to be -1.06, -0.84, and -0.7 V vs. Ag/AgCl, respectively. By conjuncting the band gap results with Mott-Schottky plots and VB-XPS spectra, the CB edges of CN, BP, and Ni₂P@BP are calculated to be -0.45, -0.34, and -0.09 V vs. SHE (standard hydrogen potential), respectively. Based on the above results, a conceptive mechanism for high H₂ production activity over Ni₂P@BP/CN is proposed. As illustrated in Fig. 6a, the excited photogenerated electron-hole pairs in CN readily migrate from the bulk to the surface owing to the thin nanosheet structures. The energetic electrons in the conduction band (CB) of CN are then consecutively transferred to the CB of BP and holes in the valence band (VB) of CN are migrated to the VB of BP owing to the straddling type 1 band alignment (Fig. 6a).

Given the excellent electron mobility of BP NSs and intimate interface among the CN, BP NSs, and Ni₂P (as discussed in Fig. 1), a large amount of photoexcited free electrons would quickly transfer from bulk CN to the surface Ni₂P catalytic active sites through the BP NSs. The abundantly present electrons on Ni₂P active sites then react with adsorbed protons to generate H₂, while the concomitant elimination of photogenerated holes by the adsorbed TEOA molecules yields oxidation reaction. These phenomena greatly increase the spatial separation of photoinduced charge carriers, and thus, accomplish better water

splitting performance. Therefore, the Ni₂P@BP co-catalyst plays at least two distinct roles simultaneously, namely, extraction and transportation of photogenerated electrons from the bulk CN, and lowering the activation barrier for the efficient reduction of H⁺ to H₂. Indeed, the TRPL, EIS, and transient photocurrent measurements (Fig. 5) of the CN, BP/CN, and Ni₂P@BP/CN samples clearly support our proposed mechanism. Based on the above interpretation, the robust photocatalytic water splitting performance of the two-dimensional Ni₂P@BP/CN can be ascribed to the following unique features, as depicted in Fig. 6b. First, two-dimensional Ni₂P@BP/CN nanocomposites with their large surface area to active sites not only enlarge the contact area between the photocatalyst and electrolyte, but also provide a short pathway for charge transportation. Second, the conductive BP NSs establish a strong ingenious interface with CN NSs, which mediates a charge separation and transfer at the BP/CN interface. This gives rise to a large number of photogenerated free electrons, which in turn leads to the enhancement in the resultant photocatalytic performance. Third, the uniform deposition of Ni₂P on BP NSs provides abundant active sites for H₂ reduction, thus avoiding the recombination of the photogenerated electron-hole pairs in CN. Overall, by virtue of the large surface area with abundant active sites, the Ni₂P@BP/CN heterostructure photocatalyst not only provides short pathways for the photoexcited charges carriers, facilitating charge transport and kinetic processes, but also accelerates the surface reduction reaction of H₂ reduction at lower overpotential, thus realizing a remarkable enhancement in the photocatalytic performance along with photo-stability for solar fuel conversion.

4. Conclusions

In summary, we proposed a heterostructured based Ni₂P@BP co-catalyst as a noble metal free co-catalyst for photocatalytic H₂ generation. The unique 2D structural configuration of the Ni₂P@BP co-catalyst endowed a large interfacial contact area, excellent electronic conductivity, and large exposed catalytic active sites for HER reaction. When the Ni₂P@BP was rationally integrated with 2D mesoporous graphitic carbon nitride, the 2D-Ni₂P@BP/CN composite photocatalysts displayed excellent visible light photocatalytic H₂ production activity of 858.2 $\mu\text{mol g}^{-1} \text{h}^{-1}$, along with exceptional stability. The experimental results revealed that the unusual photocatalytic activity of Ni₂P@BP/CN highlights the synergistic effect of efficient charge separation and transportation from CN to Ni₂P@BP and rapid proton reduction on the Ni₂P active sites to evolve H₂. Most importantly, the large lateral size of 2D Ni₂P@BP leads to extended interfacial contact with the CN photocatalyst, which remarkably reduces the charge transport pathways, and thus, provides rapid interfacial charge transfer in this unique 2D nano-architecture. Our study represents a versatile strategy to construct various highly efficient heterostructured co-catalysts as an alternative to the expensive Pt, and motivates the development of next generation, highly efficient, and inexpensive photocatalytic materials for water splitting and environmental remediation.

Acknowledgements

This work was supported by a National Research Foundation of Korea (NRF) grant funded by the Korean government (MSIP) (2012R1A3A2026417).

Appendix A. Supplementary data

Supplementary material related to this article can be found, in the online version, at doi:<https://doi.org/10.1016/j.apcatb.2018.10.018>.

References

- [1] S. Chen, T. Takata, K. Domen, Nat. Rev. Mater. 2 (2017) 17050.
- [2] X. Chen, S. Shen, L. Guo, S.S. Mao, Chem. Rev. 110 (2010) 6503–6570.

[3] R. Boppella, S.T. Kochuveedu, H. Kim, M.J. Jeong, F. Marques Mota, J.H. Park, D.H. Kim, *ACS Appl. Mater. Interfaces* 9 (2017) 7075–7083.

[4] A.J. Bard, M.A. Fox, *Acc. Chem. Res.* 28 (1995) 141–145.

[5] A. Kudo, Y. Misaki, *Chem. Soc. Rev.* 38 (2009) 253–278.

[6] K. Takanabe, *ACS Catal.* 7 (2017) 8006–8022.

[7] B.A. Pinaud, J.D. Benck, L.C. Seitz, A.J. Forman, Z. Chen, T.G. Deutsch, B.D. James, K.N. Baum, G.N. Baum, S. Ardo, H. Wang, E. Miller, T.F. Jaramillo, *Energy Environ. Sci.* 6 (2013) 1983–2002.

[8] R. Boppella, C.H. Choi, J. Moon, D.H. Kim, *Appl. Catal. B: Environ.* 239 (2018) 178–186.

[9] S. Cao, J. Yu, *J. Phys. Chem. Lett.* 5 (2014) 2101–2107.

[10] J. Zhang, Y. Chen, X. Wang, *Energy Environ. Sci.* 8 (2015) 3092–3108.

[11] L. Ma, H. Fan, M. Li, H. Tian, J. Fang, G. Dong, *J. Mater. Chem. A* 3 (2015) 22404–22412.

[12] L. Ma, H. Fan, J. Wang, Y. Zhao, H. Tian, G. Dong, *Appl. Catal. B: Environ.* 190 (2016) 93–102.

[13] Z. Yun, L. Lihua, W. Bo, W. Xinchen, *Angew. Chem. Int. Ed.* 54 (2015) 12868–12884.

[14] W.-J. Ong, L.-L. Tan, Y.-H. Ng, S.-T. Yong, S.-P. Chai, *Chem. Rev.* 116 (2016) 7159–7329.

[15] J. Yang, D. Wang, H. Han, C. Li, *Acc. Chem. Res.* 46 (2013) 1900–1909.

[16] J. Ran, J. Zhang, J. Yu, M. Jaroniec, S.Z. Qiao, *Chem. Soc. Rev.* 43 (2014) 7787–7812.

[17] C. Li, Y. Du, D. Wang, S. Yin, W. Tu, Z. Chen, M. Kraft, G. Chen, R. Xu, *Adv. Funct. Mater.* 27 (2017) 1604328.

[18] Z. Sun, H. Zheng, J. Li, P. Du, *Energy Environ. Sci.* 8 (2015) 2668–2676.

[19] P. Jiang, Q. Liu, Y. Liang, J. Tian, A.M. Asiri, X. Sun, *Angew. Chem. Int. Ed.* 53 (2014) 12855–12859.

[20] X.-D. Wang, Y.-F. Xu, H.-S. Rao, W.-J. Xu, H.-Y. Chen, W.-X. Zhang, D.-B. Kuang, C.-Y. Su, *Energy Environ. Sci.* 9 (2016) 1468–1475.

[21] D.E. Schipper, Z. Zhao, A.P. Leitner, L. Xie, F. Qin, M.K. Alam, S. Chen, D. Wang, Z. Ren, Z. Wang, J. Bao, K.H. Whitmire, *ACS Nano* 11 (2017) 4051–4059.

[22] S. Cao, C.J. Wang, W.F. Fu, Y. Chen, *ChemSusChem* 10 (2017) 4306–4323.

[23] S. Bai, W. Yin, L. Wang, Z. Li, Y. Xiong, *RSC Adv.* 6 (2016) 57446–57463.

[24] L. Zhong-Zhen, Z. Yu, Z. Chaohua, T.H. Teng, L. Zhong, A. Anas, W. Xing-Long, X. Qihu, K.K. Aik, H. Kedar, X. Jianwei, H.H. Hoon, Y. Qingyu, *Adv. Energy Mater.* 7 (2017) 1601285.

[25] M. Kaneko, I. Okura, *Photocatalysis: Science and Technology*, Springer, Heidelberg, 2002.

[26] K. Chang, Z. Mei, T. Wang, Q. Kang, S. Ouyang, J. Ye, *ACS Nano* 8 (2014) 7078–7087.

[27] J.C. Matsubu, E.T. Lin, K.L. Gunther, K.N. Bozhilov, Y. Jiang, P. Christopher, *Catal. Sci. Technol.* 6 (2016) 6836–6844.

[28] Q. Xiang, J. Yu, M. Jaroniec, *J. Am. Chem. Soc.* 134 (2012) 6575–6578.

[29] R. Boppella, J.E. Lee, F.M. Mota, J.Y. Kim, Z.X. Feng, D.H. Kim, *J. Mater. Chem. A* 5 (2017) 7072–7080.

[30] Y. Shi, B. Zhang, *Chem. Soc. Rev.* 45 (2016) 1529–1541.

[31] L. Ma, H. Fan, K. Fu, S. Lei, Q. Hu, H. Huang, G. He, *ACS Sustain. Chem. Eng.* 5 (2017) 7093–7103.

[32] B. Munkhbayar, B.E. Munkhjargal, S.J. G, *Adv. Energy Mater.* 8 (2018) 1701832.

[33] R. Xiaohui, Z. Jie, Q. Xiang, L. Yundan, H. Zongyu, L. Zhongjun, G. Yanqi, D.S. Chander, P.J. Sophia, W. Shuangyin, Z. Jianxin, Z. Han, *Adv. Energy Mater.* 7 (2017) 1700396.

[34] R. He, J. Hua, A. Zhang, C. Wang, J. Peng, W. Chen, J. Zeng, *Nano Lett.* 17 (2017) 4311–4316.

[35] W. Shuxing, H.K. San, H.K. Nam, *Adv. Sci.* 5 (2018) 1700491.

[36] J. Ran, W. Guo, H. Wang, B. Zhu, J. Yu, S.Z. Qiao, *Adv. Mater.* 30 (2018) e1800128.

[37] R. Jingrun, Z. Bicheng, Q. Shi-Zhang, *Angew. Chem. Int. Ed.* 56 (2017) 10373–10377.

[38] M. Zhu, S. Kim, L. Mao, M. Fujitsuka, J. Zhang, X. Wang, T. Majima, *J. Am. Chem. Soc.* 139 (2017) 13234–13242.

[39] M. Zhu, Y. Osakada, S. Kim, M. Fujitsuka, T. Majima, *Appl. Catal. B: Environ.* 217 (2017) 285–292.

[40] W. Jiahong, L. Danni, H. Hao, Y. Na, Y. Bo, W. Min, W. Xin, C.P. K, Y. Xue-Feng, *Angew. Chem. Int. Ed.* 57 (2018) 2600–2604.

[41] Y. Lin, Y. Pan, J. Zhang, *Int. J. Hydrogen Energy* 42 (2017) 7951–7956.

[42] L. Chunmei, D. Yonghua, W. Damping, Y. Shengming, T. Wenguang, C. Zhong, K. Markus, C. Gang, X. Rong, *Adv. Funct. Mater.* 27 (2017) 1604328.

[43] T. Su, Q. Shao, Z. Qin, Z. Guo, Z. Wu, *ACS Catal.* 8 (2018) 2253–2276.

[44] M. Yoon, Y. Oh, S. Hong, J.S. Lee, R. Boppella, S.H. Kim, F. Marques Mota, S.O. Kim, D.H. Kim, *Appl. Catal. B: Environ.* 206 (2017) 263–270.

[45] Y. Sun, S. Gao, F. Lei, Y. Xie, *Chem. Soc. Rev.* 44 (2015) 623–636.

[46] S. Illa, R. Boppella, S.V. Manorama, P. Basak, *J. Phys. Chem. C* 120 (2016) 18028–18038.

[47] K. Lingqiao, J. Yujin, D. Zhenzhen, Y. Junqing, L. Ping, L. Youyong, L. Shengzhong, *Adv. Funct. Mater.* 28 (2018) 1800668.

[48] D. Zeng, W.-J. Ong, H. Zheng, M. Wu, Y. Chen, D.-L. Peng, M.-Y. Han, *J. Mater. Chem. A* 5 (2017) 16171–16178.

[49] A.P. Grosvenor, M.C. Biesinger, R.S.C. Smart, N.S. McIntyre, *Surf. Sci.* 600 (2006) 1771–1779.

[50] L.-A. Stern, L. Feng, F. Song, X. Hu, *Energy Environ. Sci.* 8 (2015) 2347–2351.

[51] Z. Zhang, K. Liu, Z. Feng, Y. Bao, B. Dong, *Sci. Rep.* 6 (2016) 19221.

[52] W. Wang, T. An, G. Li, D. Xia, H. Zhao, J.C. Yu, P.K. Wong, *Appl. Catal. B: Environ.* 217 (2017) 570–580.

[53] P. Qiu, C. Xu, N. Zhou, H. Chen, F. Jiang, *Appl. Catal. B: Environ.* 221 (2018) 27–35.

[54] B. Tian, B. Tian, B. Smith, M.C. Scott, R. Hua, Q. Lei, Y. Tian, *Nat. Commun.* 9 (2018) 1397.

[55] I. Arindam, A. Amitava, M.P. W, M. Christoph, H. Dirk, S. Michael, A. Mesut, F. Aleksei, L. Stefan, T. Arne, D. Matthias, *Angew. Chem. Int. Ed.* 56 (2017) 1653–1657.

[56] P. Ye, X. Liu, J. Iocozzia, Y. Yuan, L. Gu, G. Xu, Z. Lin, *J. Mater. Chem. A* 5 (2017) 8493–8498.

[57] M. Schwarze, D. Stellmach, M. Schroder, K. Kailasam, R. Reske, A. Thomas, R. Schomacker, *Phys. Chem. Chem. Phys.* 15 (2013) 3466–3472.

[58] Z. Zhenyi, H. Yingzhou, L. Kuichao, G. Lijiao, Y. Qing, D. Bin, *Adv. Mater.* 27 (2015) 5906–5914.

[59] X. Wang, C. Liow, A. Bisht, X. Liu, T.C. Sum, X. Chen, S. Li, *Adv. Mater.* 27 (2015) 2207–2214.

[60] W.-J. Ong, L.K. Putri, Y.-C. Tan, L.-L. Tan, N. Li, Y.H. Ng, X. Wen, S.-P. Chai, *Nano Res.* 10 (2017) 1673–1696.

[61] R. Boppella, A. Mohammadpour, S. Illa, S. Farsinezhad, P. Basak, K. Shankar, S.V. Manorama, *Acta Mater.* 119 (2016) 92–103.

[62] L. Kong, Y. Ji, Z. Dang, J. Yan, P. Li, Y. Li, S.F. Liu, *Adv. Funct. Mater.* 28 (2018) 1800668.

[63] J. Ran, G. Gao, F.-T. Li, T.-Y. Ma, A. Du, S.-Z. Qiao, *Nat. Commun.* 8 (2017) 13907.